Estimating the magnetization distribution within rectangular rock samples

A. L. A. Reis,[1] V. C. Oliveira Jr.,[1] E. Yokoyama,[2] A. C. Bruno[3] and Pereira, J. M. B.[3]

Abstract.

Over the last decades, scanning magnetic microscopy techniques have been increasingly used in paleomagnetism and rock magnetism. Different from standard paleomagnetic magnetometers, scanning magnetic microscopes produce high-resolution maps of the vertical component of the magnetic induction field on a plane located over the sample. These high-resolution magnetic maps can be used for estimating the magnetization distribution within a rock sample by inversion. Previous studies have estimated the magnetization distribution within rock samples by inverting the magnetic data measured on a single plane above the sample. Here we present a new spatial domain method for inverting the magnetic induction measured on four planes around the sample in order to retrieve its internal magnetization distribution. We have presumed that the internal magnetization distribution of the sample varies along one of its axes. Our method approximates the sample geometry by an interpretation model composed of a one-dimensional array of juxtaposed rectangular prisms with uniform magnetization. The Cartesian components of the magnetization vector within each rectangular prism are the parameters to be estimated by solving a linear inverse problem. Tests with synthetic data show the performance of our method in retrieving complex magnetization distributions even in the presence of magnetization heterogeneities. We have also applied our method to invert experimentally measured magnetic data produced by a highly-magnetized synthetic sample that was manufactured in the laboratory. The results show that, even in the presence of apparent position noise, our method was able to retrieve the magnetization distribution consistent with the anhysteric remanance magnetization induced in the sample.

1. Introduction

Based on the estimation of the total (bulk) remanent magnetization, the standard paleomagnetic techniques have been used for more than 40 years in studies of rock magnetism, magnetostratigraphic and paleogeographic reconstructions [*Van Der Voo*, 1993]. These techniques are well established and are applied successfully in almost all paleomagnetic studies. However, this classical method has constraints in studies that need high spatial or temporal resolution, such as the secular variation's investigation. In this context, new methods have been developed over the last decades to get around these limitations, in special, the Scanning Magnetic Microscopy (SMM) techniques [*Oda et al.*, 2011; *Fu et al.*, 2014]. Different from standard paleomagnetic magnetometers, the SMM devices produce high-resolution maps of the vertical component of the magnetic induction field on a planar surface located over the sample. Usually, the scanning magnetic microscopes based on superconducting quantum interference device (SQUID) sensors achieve the best

[1]Department of Geophysics, Observatório Nacional, Rio de Janeiro, RJ, Brazil.

[2]Institute of Geosciences, University of Brasília, Brasília, DF, Brazil.

[3]Department of Physics, Pontifical Catholic University of Rio de Janeiro, Rio de Janeiro, RJ, Brazil.

field sensitivity for geoscientific research. However, these devices are very expensive to build/operate and require specific technologies to keep the sensor at cryogenic temperatures and also present a limited sensor-to-sample distance $\approx 100 \ \mu m$ [*Baudenbacher et al.*, 2003; *Fong et al.*, 2005]. Despite of these technical difficulties, SQUID sensors have been successfully applied in several paleomagnetic studies [*Gattacceca et al.*, 2006; *Weiss et al.*, 2007a; *Oda et al.*, 2011; *Fu et al.*, 2014]. To avoid the problems related with the SQUID complexity, numerous studies have been attempted to develop alternative low-cost high-performance SMM instruments based on magneto-impedance (MI) [*Uehara and Nakamura*, 2007, 2008], giant magnetoresistance (GMR) [*Hankard et al.*, 2009] and magnetic tunnel junction (MTJ) [*Lima et al.*, 2014] sensors. Compared with SQUID's, these alternative sensors are less sensitive. On the other hand, they are generally easier to operate, operate at room temperature, may achieve higher spatial resolution and also a reduction in the sensor-to-sample distance.

Paleomagnetic techniques usually separate the original rock sample mechanically and estimate the magnetization of resultant small sub-samples. In contrast, SMM allows a non-destructive characterization of the internal magnetization distribution of rock samples by inverting high-resolution magnetic data that is measured around the sample. SMM may provide huge data sets and, consequently, the inverse problems aiming at estimating the magnetization within the samples require efficient matrix algorithms. It is also well known that inverse problems aiming at estimating the magnetization distribution in planar or 3D, e.g., cylindrical and rectangular, rock samples are generally non-unique owing to an infinite number of magnetization distributions produce the same observed field. Moreover, the observed magnetic data are always noise-corrupted and is measured by magnetic sensors having limited sensitivity [*Egli and Heller*, 2000; *Baratchart et al.*, 2013; *Lima et al.*, 2013], contributing to the ill-conditioning of such inverse problems. The inherent ill-conditioning of such inverse problems can be narrowed, for example, by introducing *a priori* information regarding the magnetization distribution and/or by optimizing the geometry of the data acquisition. The introduction of *a priori* information aiming at constraining the possible estimated magnetization distributions and also making them stable to small changes in the observed data is generally called regularization [*Tikhonov and Arsenin*, 1977; *Engl et al.*, 1996; *Aster et al.*, 2005]. The regularization in the wavenumber domain is generally more tricky than in the space domain. On the other hand, methods in space domain require the solution of large-scale linear systems whereas those ones in wavenumber domain take advantage of the Fast Fourier Transform (FFT) algorithms.

Generally, SMM paleomagnetic studies estimate the approximately 2D magnetization distribution within planar rock samples (usually thin sections) by inverting the magnetic data measured on a parallel plane located over it. The pioneer study of *Egli and Heller* [2000] presents a method, in the wavenumber domain, aiming at retrieving the particular magnetization component that is perpendicular to the planar sample. These authors adapted the method proposed by *Mareschal* [1985] and formulated their problem as a two-dimensional deconvolution, which is solved by applying the FFT. By following a similar approach in the wavenumber domain, *Lima et al.* [2013] presented an efficient method attempted to estimate the magnetization intensity distribution within a planar rock sample having a previously defined constant

magnetization direction. The method developed by *Lima et al.* [2013] also uses two-dimensional signal processing methods to regularize the inverse problem, tame noise amplification and improve non-negativity.

A different approach proposed by [*Weiss et al.*, 2007b] in space domain approximates the sample by a discrete set of dipoles. The Cartesian components of the dipoles approximating the sample are estimated by iteratively solving a large linear inverse problem. This method is an adaptation of the well-known equivalent layer technique, which has long been applied to processing potential-field data in space domain [*Dampney*, 1969; *Emilia*, 1973; *Von Frese et al.*, 1981; *Hansen and Miyazaki*, 1984; *Silva*, 1986; *Leão and Silva*, 1989; *Cordell*, 1992; *Mendonça*, 1992; *Mendonça and Silva*, 1994, 1995; *Guspí and Novara*, 2009; *Li and Oldenburg*, 2010; *Barnes and Lumley*, 2011; *Oliveira Jr. et al.*, 2013; *Kara et al.*, 2014; *Li et al.*, 2014; *Barnes*, 2014]. The study developed by [*Weiss et al.*, 2007b] represents the first space-domain technique for inverting SMM data. *Usui et al.* [2012] presented an hybrid method combining useful features of space- and wavenumber-domain techniques. They described the magnetization distribution in a planar rock sample as a weighted average according to the Backus-Gilbert formulation. In order to overcome the computational cost of the BackusGilbert method, *Usui et al.* [2012] implemented the subtractive optimally localized averages (SOLA) method, which was originally proposed to solve large-scale inverse problems in helioseismic. The SOLA method approximates some matrix computations by using the FFT, but does not transform the magnetic data to the Fourier domain.

Here, we propose a new spatial domain inversion method to invert the magnetic induction measured on four orthogonal planes around the sample in order to retrieve its internal magnetization distribution. Our method approximates the sample by an interpretation model composed of a one-dimensional array of juxtaposed rectangular prisms with uniform magnetization. The number of rectangular prisms making up the interpretation model is specified by the interpreter and the Cartesian components of the magnetization vector within each rectangular prism are the parameters to be estimated by solving a linear inverse problem.

By imposing this finite one-dimensional magnetization distribution, we constraint the mathematically possible solutions, which results in a regularization by discretization [*Engl et al.*, 1996; *Aster et al.*, 2005]. Moreover, the use of magnetic data measured on more than one plane around the sample adds independent information about its internal magnetization distribution, which also contributes to stabilize the inverse problem. In comparison with previous methods, the method proposed here does not deal with large-scale inverse problems because our interpretation model is described by a relatively few number of parameters.

We have inverted magnetic data produced by numerical simulations with the purpose of illustrating not only the good performance of our method in ideal cases, but also how the estimated magnetization distribution obtained by our method can be negatively impacted by the presence of position noise, errors in the sensor-to-sample distance and pre-processing errors in the observed data. Tests with synthetic data simulating a real ferro-manganese crust with magnetization heterogeneities show that our method can be used, for example, in fine-scale magnetostratigraphic studies. We have also shown the results obtained by applying our method to invert experimentally measured magnetic data produced by

a highly-magnetized synthetic sample that was manufactured in laboratory. The results show that our method is able to estimate a magnetization distribution that is consistent with the Anhysteric Remanance Magnetization (ARM) induced in the sample, even by inverting a magnetic data set that is contaminated by apparent position noise and were measured by a custom-made magnetometer based on a Hall sensor.

2. Methodology

2.1. Observed data vector

Let's consider a rectangular rock sample with side lengths equal to L_x, L_y e L_z along, respectively, the x-, y- and z-axes of a Cartesian coordinate system whose origin coincides with the center of the sample (Fig. 1). This coordinate system is conveniently called "main coordinate system" (MCS). We assume that the internal magnetization distribution of the sample varies along the x-axis of the MCS. We also considered four mutually orthogonal planes that are located at the same distance h from the sample surface and are identified by an index $\alpha = 0, 1, 2, 3$ (Figs. 2 and 3). On each plane, there are N measurements of a specific β-component of the magnetic induction, $\beta = y, z$, which is perpendicular to the sample surface and is referred to the MCS.

Let $\mathbf{d}_\beta^\alpha$, $\beta = y, z$, $\alpha = 0, 1, 2, 3$, be $N \times 1$ vectors whose i-th element is the β-component of the magnetic induction which is measured at the observation point $(x_i^\alpha, y_i^\alpha, z_i^\alpha)$, $i = 1, ..., N$, on the plane α. For convenience, these vectors are all grouped into the observed data vector $\mathbf{d}$ given below:

$$\mathbf{d} = \begin{bmatrix} \mathbf{d}_z^0 \\ \mathbf{d}_y^1 \\ \mathbf{d}_z^2 \\ \mathbf{d}_y^3 \end{bmatrix}_{4N \times 1} . \qquad (1)$$

2.2. Transformations from the local coordinate systems (LCS's) to the MCS

The Cartesian coordinates as well as the magnetic induction components in the observed data vector $\mathbf{d}$ (equation 1) are referred to the MCS (Figure 1). However, the measurements are taken in a different local coordinate system (LCS) for each observation plane (Figures 3b-e) and must be subsequently converted to the MCS (Figure 3a). This coordinate transformation is needed because the usual magnetic sensors can measure the vertical component of the magnetic induction produced by the sample on a plane located over it. For this reason, the magnetic data on the four observation planes (Figure 2) are obtained by successively rotating the sample through $90°$ intervals around its major axis (x-axis in Figure 1). By repeating this rotating procedure and maintaining the same distance h between the observation plane and the sample surface, its possible to obtain the magnetic induction on the four observation planes (Figures 2). The LCS on each plane has axes x', y' and z' (Figure 3b-e), where the x'-axis coincides with the x-axis of the MCS.

Note that this rotating procedure provides, on each observation plane, the component of the magnetic induction along the z'-axis of the respective LCS (Figure 3b-e). It is easier, however, converting the measured z'-component data, as well as its Cartesian coordinates, from the LCS's to the MCS. The geometrical relationships between these coordinate systems are shown in Figure 3. Table 1 shows

how to perform this coordinate transformation. Let's consider, for example, the measurements obtained on the observation plane $\alpha = 1$ (Figures 2b and 3c). According to this table, the opposite of the measured z'-component data correspond to the y-component of the magnetic induction that would be measured in the MCS; the opposite of the Cartesian coordinates along the z'-axis correspond to the Cartesian coordinates along the y-axis in the MCS; the Cartesian coordinates along the y'-axis correspond to the Cartesian coordinates along the z-axis in the MCS. The other lines of Table 1 contain the relationships used to convert the data obtained on the other planes. Hereafter, it is implicit that all quantities with prime ($'$) are referred to the LCS's while all the quantities without prime ($'$) are referred to the MCS.

2.3. Interpretation model and forward problem

We consider that the rock sample can be approximated by an interpretation model consisting of P uniformly magnetized prisms, which are juxtaposed along the x-axis (Figure 1). The k-th prism, $k = 1, ..., P$, has the same side lengths L_y and L_z of the sample along, respectively, the y- and z-axes (Figure 1). However, its side length along the x-axis is specified by the interpreter, so that the total side length of the interpretation model along this axis is equal to L_x (Figure 1).

Let's define the $3P \times 1$ parameter vector $\mathbf{m}$ as follows:

$$\mathbf{m} = \begin{bmatrix} \mathbf{m}^1 \\ \vdots \\ \mathbf{m}^P \end{bmatrix}_{3P \times 1} , \qquad (2)$$

where

$$\mathbf{m}^k = \begin{bmatrix} m_x^k \\ m_y^k \\ m_z^k \end{bmatrix}_{3 \times 1} , \qquad (3)$$

is a 3×1 vector containing the Cartesian components m_x^k, m_y^k and m_z^k (in A/m) of the magnetization vector of the k-prism, $k = 1, \ldots, P$.

The β-component data, $\beta = y, z$, of the magnetic induction produced by the k-prism (in nT), at the observation points $(x_i^\alpha, y_i^\alpha, z_i^\alpha)$, $i = 1, ..., N$, $\alpha = 0, 1, 2, 3$, are grouped into $N \times 1$ vectors given by

$$\mathbf{b}_\beta(\mathbf{x}^\alpha, \mathbf{y}^\alpha, \mathbf{z}^\alpha, \mathbf{m}^k) = \mathbf{M}_\beta^k(\mathbf{x}^\alpha, \mathbf{y}^\alpha, \mathbf{z}^\alpha)\mathbf{m}^k , \qquad (4)$$

where

$$\mathbf{M}_\beta^k(\mathbf{x}^\alpha, \mathbf{y}^\alpha, \mathbf{z}^\alpha) = \begin{bmatrix} \partial_{\beta x}\phi^k(x_1^\alpha, y_1^\alpha, z_1^\alpha) & \partial_{\beta y}\phi^k(x_1^\alpha, y_1^\alpha, z_1^\alpha) & \partial_{\beta z}\phi^k(x_1^\alpha, y_1^\alpha, z_1^\alpha) \\ \vdots & \vdots & \vdots \\ \partial_{\beta x}\phi^k(x_N^\alpha, y_N^\alpha, z_N^\alpha) & \partial_{\beta y}\phi^k(x_N^\alpha, y_N^\alpha, z_N^\alpha) & \partial_{\beta z}\phi^k(x_N^\alpha, y_N^\alpha, z_N^\alpha) \end{bmatrix}_{N \times 3}$$
$$(5)$$

is a matrix whose elements are second derivatives of the function

$$\phi^k(x, y, z) = C_m \iiint\limits_{\vartheta^k} \frac{d\epsilon \, d\zeta \, d\eta}{\sqrt{(x - \epsilon)^2 + (y - \zeta)^2 + (z - \eta)^2}}$$
$$(6)$$

with respect to the variables x, y and z, $C_m = 10^9 \mu_0 / 4\pi$ and μ_0 is the magnetic constant. In equations 4 and 5, $\mathbf{x}^\alpha$, $\mathbf{y}^\alpha$ and $\mathbf{z}^\alpha$ are vectors containing, respectively, the Cartesian coordinates x_i^α, y_i^α and z_i^α, $i = 1, ..., N$, of the observation points on the plane α, referred to

the MCS. In this work, the second derivatives in matrix $\mathbf{M}_\beta^k(\mathbf{x}^\alpha, \mathbf{y}^\alpha, \mathbf{z}^\alpha)$ (equation 5) are calculated by using the formulas presented by *Nagy et al.* [2000]. In equation 6, the integral is evaluated over the volume ϑ^k of the k-th prism.

From equation 4, we defined the $N \times 1$ vectors $\mathbf{B}_\beta^\alpha(\mathbf{m})$ containing the resultant β-component of the magnetic induction produced by the interpretation model on each plane α as follows:

$$\mathbf{B}_\beta^\alpha(\mathbf{m}) \equiv \sum_{k=1}^{P} \mathbf{b}_\beta(\mathbf{x}^\alpha, \mathbf{y}^\alpha, \mathbf{z}^\alpha, \mathbf{m}^k) . \qquad (7)$$

By grouping all these vectors $\mathbf{B}_\beta^\alpha(\mathbf{m})$, we define the predicted data vector

$$\mathbf{B}(\mathbf{m}) = \begin{bmatrix} \mathbf{B}_z^0(\mathbf{m}) \\ \mathbf{B}_y^1(\mathbf{m}) \\ \mathbf{B}_z^2(\mathbf{m}) \\ \mathbf{B}_y^3(\mathbf{m}) \end{bmatrix}_{4N \times 1} . \qquad (8)$$

Finally, by substituting equation 4 into equation 7 and rearranging the terms within the summation, we can conveniently rewrite the predicted data vector $\mathbf{B}(\mathbf{m})$ (equation 8) as follows:

$$\mathbf{B}(\mathbf{m}) = \mathbf{M}\mathbf{m} , \qquad (9)$$

where $\mathbf{M}$ is a partitioned matrix given by

$$\mathbf{M} = \begin{bmatrix} \mathbf{M}_z^1(\mathbf{x}^0, \mathbf{y}^0, \mathbf{z}^0) & \dots & \mathbf{M}_z^P(\mathbf{x}^0, \mathbf{y}^0, \mathbf{z}^0) \\ \mathbf{M}_y^1(\mathbf{x}^1, \mathbf{y}^1, \mathbf{z}^1) & \dots & \mathbf{M}_y^P(\mathbf{x}^1, \mathbf{y}^1, \mathbf{z}^1) \\ \mathbf{M}_z^1(\mathbf{x}^2, \mathbf{y}^2, \mathbf{z}^2) & \dots & \mathbf{M}_z^P(\mathbf{x}^2, \mathbf{y}^2, \mathbf{z}^2) \\ \mathbf{M}_y^1(\mathbf{x}^3, \mathbf{y}^3, \mathbf{z}^3) & \dots & \mathbf{M}_y^P(\mathbf{x}^3, \mathbf{y}^3, \mathbf{z}^3) \end{bmatrix}_{4N \times 3P} , \qquad (10)$$

which is formed by the matrices $\mathbf{M}_\beta^k(\mathbf{x}^\alpha, \mathbf{y}^\alpha, \mathbf{z}^\alpha)$, $\beta = y, z$, $\alpha = 0, 1, 2, 3$, $k = 1, \dots, P$ (equation 5).

2.4. Inverse problem

By presuming that the rectangular rock sample can be approximated by our previously described interpretation model, we define the linear inverse problem of estimating its internal magnetization distribution as an optimization problem. This optimization problem consists in estimating a specific parameter vector $\mathbf{m} = \mathbf{m}^\dagger$ (equation 2) that minimizes the goal function

$$\Gamma(\mathbf{m}) = [\mathbf{d} - \mathbf{B}(\mathbf{m})]^\top [\mathbf{d} - \mathbf{B}(\mathbf{m})] , \qquad (11)$$

where $\mathbf{d}$ and $\mathbf{B}(\mathbf{m})$ are, respectively, the observed and predicted data vectors (equations 1 and 9). The minimization of the goal function $\Gamma(\mathbf{m})$ (equation 11) is equivalent to estimate the parameter vector minimizing the difference between the observed and predicted data vectors in the least-squares sense.

The parameter vector $\mathbf{m} = \mathbf{m}^\dagger$ minimizing the goal function (equation 11) is given by

$$\mathbf{m}^\dagger = \left(\mathbf{M}^\top \mathbf{M} \right)^{-1} \mathbf{M}^\top \mathbf{d} , \qquad (12)$$

where $\mathbf{M}$ is the partitioned matrix defined in equation 10. We consider that the estimated parameter vector $\mathbf{m}^\dagger$ given by equation 12 approximates the real magnetization distribution within the rectangular rock sample.

However, solutions given by the equation 12 can present non-uniqueness and instability. To overcome this ill-conditioning problem we need to impose a *priori* information. As mentioned before, this procedure is generally called regularization. Here we imposed a constraint using "Smoothness" regularization, generally called first-order Tikhonov regularization. Then equation 12 is now equal to

$$\mathbf{m}^{\dagger} = \left(\mathbf{M}^{\top}\mathbf{M} + \mu_0\, \mathbf{R}^{T}\mathbf{R}\right)^{-1} \mathbf{M}^{\top}\mathbf{d}\,, \qquad (13)$$

where μ_0 is a positive number called parameter regularization and $\mathbf{R}$ is a matrix with elements -1 and 1. For example, if we have a sample formed by two prisms ($P = 2$), the matrix $\mathbf{R}$ can be written as

$$\mathbf{R} = \begin{bmatrix} 1 & 0 & 0 & -1 & 0 & 0 \\ 0 & 1 & 0 & 0 & -1 & 0 \\ 0 & 0 & 1 & 0 & 0 & -1 \end{bmatrix}_{3P-3\times 3P}. \qquad (14)$$

Generally, the matrix $\mathbf{R}$ is composed by $3P = 3$ rows and $3P$ columns. Each element of the matrix can be described as

$$[\mathbf{R}]_{ij} = \begin{cases} 1\,, & i = j \\ -1\,, & j = i + 3 \end{cases}, \qquad (15)$$

where the others elements of the matrix are zero.

2.5. Pre-processing

Our method presumes that the edges of the sample are aligned with the axes of all LCS's (Figure 3b-e) and also that the center of the sample must be placed right below the origin of all LCS's. Notwithstanding, these conditions are not necessarily satisfied in practical situations. Figure 4a illustrates a situation in which these conditions are satisfied. On the other hand, Figure 4b shows a situation in which neither the horizontal coordinates of the center of the sample (black dot) coincide with the origin of the LCS (open dot), nor the edges of the sample are aligned with the axes x' and y' of the LCS. In this case, it is necessary to correct the coordinates $\tilde{x}'$ and $\tilde{y}'$ of the magnetic data on the observation plane with respect to the sample in order to positioning the sample according to the Figure 4a. This correction must be applied to the magnetic data obtained on the four observation planes.

On each observation plane, let's first denote by x'_c and y'_c the horizontal coordinates of the center of the observation plane (represented by the open dot in Figure 4b). Then, the horizontal coordinates $\tilde{x}'$ and $\tilde{y}'$ of each magnetic data on the observation plane are corrected by applying the following transformation:

$$\begin{bmatrix} x' \\ y' \end{bmatrix} = \mathbf{R}^{\top} \begin{bmatrix} \tilde{x}' - x'_c \\ \tilde{y}' - y'_c \end{bmatrix} + \begin{bmatrix} x'_c \\ y'_c \end{bmatrix} - \begin{bmatrix} \Delta x' \\ \Delta y' \end{bmatrix}, \qquad (16)$$

where $\Delta x'$ and $\Delta y'$ are the horizontal displacements of the center of the sample with respect to the origin of the respective LCS (Figure 4b),

$$\mathbf{R} = \begin{bmatrix} \cos\theta & \sin\theta \\ -\sin\theta & \cos\theta \end{bmatrix}, \qquad (17)$$

and θ (Figure 4b) is the angle between the edges of the sample and the horizontal axes x' and y' of the respective LCS. After applying this transformation for correcting the horizontal coordinates $\tilde{x}'$ and $\tilde{y}'$ of each magnetic data on a observation plane, we obtain the corrected coordinates x' and y', which are placed on a different area represented by the grey rectangle in Figure 4c.

This transformation must be applied to the magnetic

data on the four observation planes, before the previously described transformations from the LCS's to the MCS. We would like to stress that the transformation described in equations 16 and 17 requires the knowledge of the angle θ and also the displacements $\Delta x'$ and $\Delta y'$ (Figure 4b). In practical situations, these values are easily estimated by trial-and-error. Finally, on each observation plane, the magnetic data are subtracted from its mean value in order to remove the effect of a possible (weak) interfering field.

2.6. Sensor active area

Magnetic sensors do not measure the magnetic induction field at a point. They measure instead the field averaged over the sensor active area (or volume), which is equivalent to a convolution of the magnetic induction field with the sensor answer function [*Roth et al.*, 1989; *Egli and Heller*, 2000; *Lima et al.*, 2013]. The sensor-to-sample distance and the effective area (or volume) are important limiting factors determining the spatial resolution of magnetic sensors.

The magnetic sensors used in paleomagnetic applications have different active area (or volume). *Uehara and Nakamura* [2007, 2008] presented a magneto-impedance (MI) sensor whose cylindrical active volume has 36μm in diameter and 5500μm in length, which limits its spatial resolution if compared with the giant magnetoresistance (GMR) sensor presented by *Hankard et al.* [2009] and the magnetic tunnel junction (MTJ) sensor presented by *Lima et al.* [2014], for example. These two sensors are considered planar and have active areas of, respectively, 9μm $\times$ 36μm and $\approx 4\mu$m $\times 2\mu$m. Finally, *Fong et al.* [2005] presented a low-transition-temperature superconducting quantum interference device (low T$_c$ SQUID) sensor which is also considered planar and has an active area with diameter of 80μm. This is currently one of the most powerful magnetic sensors.

In the following, we present an analysis of the averaging effect produced by the finite size of sensors. We limit our study to squared-planar sensors which are parallel to the sample surface. Let us first consider the magnetic induction component $\tilde{b}(x, y)$ that is parallel to the sample surface and is threaded through a planar sensing area parallel to the sample as the following two-dimensional convolution

$$\tilde{b}(x,y) = \int\limits_{-\infty}^{\infty} \int\limits_{-\infty}^{\infty} w(\eta, \zeta)\, b(x - \eta, y - \zeta)\, d\eta d\zeta\,, \quad (18)$$

where $w(\eta, \zeta)$ is the sensor answer function [*Egli and Heller*, 2000]. Here, we do not consider the dependence with the sensor-to-sample distance h (Figure 5a). For convenience, we consider a square sensor having an active area A (light grey square in Figure 5a). In this case, the sensor answer function $w(\eta, \zeta)$ is given by [*Egli and Heller*, 2000]

$$w(x,y) = \begin{cases} 1/A\,, & (x,y) \in A \\ 0\,, & (x,y) \notin A \end{cases} \quad . \quad (19)$$

By substituting this sensor answer function into the magnetic flux integral (equation 18) we obtain

$$\tilde{b}(x,y) = \frac{1}{A} \int\limits_{-\infty}^{\infty} \int\limits_{-\infty}^{\infty} b(x - \eta, y - \zeta)\, d\eta d\zeta\,. \quad (20)$$

Equation 20 has an analytical solution in the wavenumber domain [*Egli and Heller*, 2000]. However, we opted for using an approximated solution in the space domain. This approximation consists in discretizing the integral 20 by using a midpoint rule on a regular grid of $Q_x \times Q_y$ points $(x_j, y_j) \in A$, $j = 1, ..., n$, where $Q = Q_x Q_y$. The approximated integral is given by

$$\tilde{b}_i \approx \frac{\Delta A}{A} \sum_{j=1}^{Q} b_j \,, \tag{21}$$

where $\tilde{b}_i \equiv \tilde{b}(x_i, y_i)$, (x_i, y_i) is the point located at the center of the sensor active area A (black circle in Figure 5b) and b_j is the magnetic induction component parallel to the sample surface and evaluated at the point (x_j, y_j) (open circle in Figure 5c), $j = 1, ..., Q$. According to the discretization represented in Figure 5b, the active sensor area is divided into a regular grid of square cells with area ΔA (Figure 5c). Hence, by noting that $A = Q \, \Delta A$, we get

$$\tilde{b}_i \approx \frac{1}{Q} \sum_{j=1}^{Q} b_j \,. \tag{22}$$

Equation 22 shows that the magnetic induction $\tilde{b}_i$ at the observation point (x_i, y_i) is approximately given by the magnetic induction averaged over the active area A of the sensor.

3. Numerical simulations

3.1. Highly magnetized sample

We have applied our method to invert the synthetic data produced by a simulated rock sample (not shown) with $L_x = 16$ mm and $L_y = L_z = 3$ mm, according to the Figure 1. This synthetic sample is formed by $P = 16$ juxtaposed prisms along the x-axis, where each prism has a uniform and high magnetization (red dots in Figures 7, 9 and 11). In all tests presented in this section, the magnetic data produced by the synthetic sample on each plane α, $\alpha = 0, 1, 2, 3$, were calculated on a regular grid of 102×42 points along the x and y/z axes, respectively, and were also contaminated with a pseudo-random Gaussian noise having null mean and standard deviation equal to $30,000$ μT. These data simulate an observed data set. Besides, we have simulated the misalignment problems described in the subsection 2.5. Table 2 shows the parameters θ, $\Delta x'$ and $\Delta y'$ (Figure 4b) representing these misalignments in the magnetic data produced by the synthetic sample on the planes $\alpha = 0, 1, 2, 3$.

3.1.1. Validation test

In this test, the simulated noise-corrupted data were calculated by keeping the distance h (Figure 3) between all the planes and the surface of the sample equal to 500 μm. The noise-corrupted magnetic data were properly corrected from the misalignment problems by using the parameters shown in Table 2 and the equations 16 and 17. These magnetic data (Figures 6a, d, g and j) were inverted by our method in order to retrieve the internal magnetization distribution of the synthetic sample (red dots in Figures 7, 9 and 11). To do that, we used an interpretation model which has side lengths L_x, L_y and L_z equal to the true ones and is formed by the same number of prisms ($P = 16$) as the synthetic sample.

Figure 7 shows that the estimate obtained with our method (blue dots) successfully retrieved the magnetization distribution of the simulated sample (red dots). This estimated magnetization distribution yields a predicted data (Figures 6b, e, h and k) that is very close to

the observed data (Figures 6a, d, g and j). The normalized histograms of the residuals between the predicted and observed data (Figures 6c, f, i and l) show sample means μ and sample standard deviations σ very close to that ones of the pseudo-random noise contaminating the simulated magnetic data.

These results show the good performance obtained by our method if all the premises about the magnetic data and the sample are not violated.

3.1.2. Pre-processing errors

As in the previous test, the simulated noise-corrupted data used here were calculated by keeping the distance h (Figure 3) between all the planes and the surface of the sample equal to 500 μm. On the other hand, we have not corrected the misalignment problems by using the parameters shown in Table 2 and the equations 16 and 17. We have also introduced a different constant bias into the misaligned magnetic data on each plane with the purpose of simulate errors in the pre-processing stage. These bias are equal to $-26,000$ μT, $-10,000$ μT, $-26,000$ μT and $-23,000$ μT for the magnetic data on the planes $\alpha = 0, 1, 2$ and 3, respectively. As in the previous test, we applied our method by using an interpretation model with side lengths L_x, L_y and L_z equal to the true ones and with the same number of prisms ($P = 16$) as the synthetic sample along the x-axis.

Figure 9 shows that, differently from the previous test, the estimate obtained with our method (blue dots) failed in retrieving the magnetization distribution of the simulated sample (red dots). This poorly-estimated magnetization distribution yields predicted data (Figures 8b, e, h and k) that do not recover the observed data (Figures 8a, d, g and j). This coarse data fit is shown by the normalized histograms of the residuals between the predicted and observed data (Figures 8c, f, i and l). The sample means μ would be very close to the simulated constant bias and the sample standard deviations σ would be very close to that one of the pseudo-random noise if the magnetic data were properly corrected from the misalignment problems.

These results exemplify the effects of not correcting the misalignment problems prior to the inversion. As we can see, these problems lead to an estimated magnetization distribution that do not retrieves the true one and also produce a coarse data fit.

3.1.3. Sensor-to-sample distance

Unlike the previous tests, the simulated noise-corrupted data used here were calculated at a different distance h (Figure 3) between each observation plane and the surface of the sample. The distances h between the sample surface and the planes $\alpha = 0, 1, 2$ and 3 are equal to 420 μm, 330 μm, 400 μm and 230 μm, respectively. The noise-corrupted magnetic data were properly corrected from the misalignment problems by using the parameters shown in Table 2 and the equations 16 and 17. As in the previous tests, we applied our method by using an interpretation model with side lengths L_x, L_y and L_z equal to the true ones and with the same number of prisms ($P = 16$) as the synthetic sample along the x-axis. We have applied our method to invert the noise-corrupted magnetic data without, however, consider the variations in the sensor-to-sample distances h. Instead, we presumed a constant distance $h = 500$ μm between all the planes and the surface of the sample.

Figure 11 shows that the estimate obtained with our method (blue dots) did not completely retrieved the magnetization distribution of the synthetic sample (red dots), but is much better than that one obtained in the previous test (blue dots in Figure 9). This (almost good) estimated

magnetization distribution yields predicted data (Figures 10b, e, h and k) that recover the observed data (Figures 10a, d, g and j) in an acceptable manner. This acceptable data fit is shown by the normalized histograms of the residuals between the predicted and observed data (Figures 10c, f, i and l). The sample means μ are close to zero but the sample standard deviations σ present some discrepancies with respect to that one of the pseudo-random noise in magnetic data. According to these histograms, the poorest data fit occurs in the observation plane $\alpha = 3$ (Figure 10l), where the sample standard deviation $\sigma \approx 42$ μT.

These results illustrate the effects of errors in the sensor-to-sample distance. If compared with the results obtained in the previous test, the results obtained here suggest that our method is most robust against errors in the sensor-to-sample distance than against misalignment errors.

3.2. Marine ferro-manganese crust sample

The method proposed by *Oda et al.* [2011] uses SQUID microscopy to identify the boundaries of fine magnetic stripes (smaller than 1 mm) with approximately reversed magnetization. These magnetic stripes are then correlated with a standard magneto-stratigraphic time scale, providing a tool for estimating ages and growth rates for hydro-genetic ferro-manganese crusts with unprecedented spatial resolution. *Oda et al.* [2011] applied their method to analyse a block of ferro-manganese crust obtained from a seamount in the Northwest Pacific Ocean. They have cut and sliced a columnar block parallel to the growth lamination at 1.5 mm intervals using a 0.3-mm-thick diamond-wire saw. After that, the magnetization of the slices have been estimated by using a SQUID magnetometer. Note that, to determine the magnetization along the sample, it was necessary to slice it in small parts. It would be useful instead to determine the bulk magnetization along the sample by using a non-destructive method. Here, we present a feasibility study aiming at determining the magnetization distribution along a simulated sample by applying our method and directly inverting the high-resolution measurements of the magnetic induction around the sample.

The internal magnetization distribution of our simulated sample is based on the real magnetization distribution within the ferro-manganese crust presented by *Oda et al.* [2011]. Our sample (not shown) is formed by $P = 24$ juxtaposed prisms along the x-axis and has side lengths equal to $L_x = 36$ mm, $L_y = 5$ mm and $L_z = 5$ mm along, respectively, the x, y and z axes. Figure 13 shows the magnetization of these prisms (red dots) along the x-axis of the sample. We have also simulated the presence of 20 magnetized grains that are randomly placed within the sample. These grains are represented by spheres having radius equal to 30 μm, constant magnetization intensity of 100 A/m and random magnetization direction. The magnetic data produced by our heterogeneous sample on each plane $\alpha = 0, 1, 2, 3$ were calculated at a constant distance $h = 370$ μm, on a regular grid of 200×100 points along the x and y/z axes, respectively, and were also contaminated with a pseudo-random Gaussian noise having null mean and standard deviation equal to 1.0 nT (Figures 12a, d, g and j).

Figure 13 shows that the estimate obtained with our method (blue dots) completely retrieved the magnetization distribution of the simulated heterogeneous sample (red dots). This estimated magnetization distribution yields a predicted data (Figures 12b, e, h and k) that is very close to the observed data (Figures 12a, d, g and

j), except at the regions where the simulated spherical grains are close to the sample surface. The normalized histograms of the residuals between the predicted and observed data (Figures 12c, f, i and l) show sample means μ and sample standard deviations σ very close to that ones of the pseudo-random noise contaminating the simulated magnetic data.

These results confirm the good performance of our method in retrieving the magnetization distribution within a complex and heterogeneous synthetic sample simulating a real ferro-manganese crust.

4. Tentative application to real data produced by a synthetic sample

4.1. Sample preparation

We have applied our method to invert experimentally measured data produced by a highly magnetized sample (not shown) that was manufactured in the laboratory of Paleomagnetism of the Institute of Geophysics, Astronomy and Atmospheric Sciences of the University of São Paulo (IAG-USP), in Brazil. The sample is formed by four juxtaposed prisms with side lengths equal to ≈ 4 mm, ≈ 3 mm and ≈ 3 mm along, respectively, the x-, y- and z-axis (with respect to the MCS shown in Figure 1). These prisms were manufactured by filling a rectangular acrylic mould with a magnetite solution and letting it harden. The magnetite solution is formed by a mixture of a diamagnetic epoxy resin and colloidal magnetite obtained from the reaction of ferric sulphate and ferrous chloride. The hardened prisms were then magnetized anhysteretically by an inducing field of ≈ 1T, according to the schematic representation shown in Figures 14a and b. Finally, the prisms were juxtaposed (Figure 14c), resulting in a sample with side lengths equal to $L_x \approx 16$ mm, $L_y \approx 3$ mm and $L_z \approx 3$ mm. The inclination and declination values of the ARM magnetization within each prism are shown in Table 3.

4.2. Data acquisition

The magnetic induction data on the four observation planes around our synthetic sample were measured by a scanning Hall magnetic microscope, developed at Pontifical Catholic University of Rio de Janeiro (PUC-Rio), in Brazil. It is based on a commercial GaAs Hall-effect sensor (HG-176A, AKM Inc.) that detects the remanent magnetic field normal to the scanning plane. The sensor has an active area size of $300\,\mu m$, which is $250\,\mu m$ distant from the top of the encapsulation. The maximum spatial resolution achieved is about the size of the sensors active area. The magnetic field sensitivity measured is $350\,nT/Hz^{1/2}$ in the white noise region. The sensor is current biased and pre-amplified by a custom-made electronics at $1.0\,kHz$, and the output Hall voltage is detected by a lock-in amplifier. In our microscope, two independent linear micropositioners (T-LLS260, Zaber Technologies) were oriented perpendicularly and stacked, making up an $x-y$ stage with a maximum travel range of $50\,mm$ in each direction. An acrylic pedestal, $15\,mm$ long, is fixed to the stage, serving two purposes, providing a flat surface for the sample to be mounted to and increasing the distance from the sample to the micropositioners motors minimizing inductive effects. The sensor is mounted on another acrylic rod that can be raised or lowered using a linear actuator (T-LA60A, Zaber Technologies), allowing for the adjustment of the sensor to sample distance with micrometer accuracy. The scanning of the sample is made in a stop-and-go system, meaning

that when the sample is moved to a scanning position, it stops for the magnetic field measurement and only then, it goes to the next position. In order to reduce environmental magnetic noise present at the laboratory, the experimental measurements were made inside a small 3 layer open-end magnetic shielded chamber (TLM S-0100, Bartington Instruments). We used for scanning a step of $200 \, \mu m$ in both x and y directions. On each plane $\alpha = 0, 1, 2, 3$, the magnetic data were measured at a constant distance $h \approx 500 \, \mu$m, on a regular grid of 102×42 points along the x and y/z axes, respectively (Figures 15a, d, g and j). The observed magnetic data were corrected from the apparent misalignment problems by testing different combinations of parameters θ, $\Delta x'$ and $\Delta y'$ (Figure 4b and equations 16 and 17). The best parameters are very close to those ones shown in Table 2. After that, the magnetic data sets obtained on each plane were subtracted from their respective mean values.

4.3. Results and comments

We inverted the observed magnetic data by using an interpretation model which is formed by $P = 16$ prisms and has side lengths equal to $L_x = 16$ mm, $L_y = 3$ mm and $L_z = 3$ mm along, respectively, the x, y and z axes. Note that each prism forming the synthetic sample is approximated by four juxtaposed prisms of the interpretation model. Figure 16 shows the estimated magnetization distribution obtained with our method. This estimated magnetization distribution yields a predicted data (Figures 15b, e, h and k) that recover the main features in the observed data (Figures 15a, d, g and j). This coarse data fit is shown by the normalized histograms of the residuals between the predicted and observed data (Figures 15c, f, i and l). These histograms show non-null sample means μ and different sample standard deviations σ.

Based on the results obtained with synthetic data, this poor data fit may be related to the misalignment problems. Probably, the parameters θ, $\Delta x'$ and $\Delta y'$ (Figure 4b and equations 16 and 17), which were estimated by trial-and-error, do not lead to a suitable correction of the misalignment problems. These problems, however, were possibly worsened by the apparent imprecision in the sensor positioning (or position noise) during the scanning stage. According to *Lee et al.* [2004], the presence of position noise has an important implication for the design of scanning magnetic microscopy. We have also verified with synthetic data that errors in the sensor-to-sample distance could negatively impact the results obtained by our method.

These results cannot nonetheless be completely rejected owing to the estimated magnetization distribution along the synthetic sample shows two important characteristics.

The first one concerns the estimated magnetization intensities (Figure 16a). As we can see, the estimated intensities exhibit an interesting pattern formed by a well-defined cycle of a low value that is followed by three higher values. This cycle repeats four times, coinciding with the number of prisms forming our synthetic sample. For convenience, grouped the estimated values representing the magnetization within each prism. The low values observed in the estimated magnetization intensities (Figure 16a), as well as the corresponding inclination and declination values (Figures 16b and c), are represented by black triangles. This remarkable pattern is consistent with the magnetite precipitation during the manufacturing of our sample. This precipitation would decrease the magnetite concentration at the top

of each sample prism, increasing the concentration towards their bottom. The magnetic induction produced by these low-concentration zones there must be superimposed by those ones produced by the high-concentration zones, which makes the correct estimation of the magnetization direction in these low-concentration zones very difficult. Due to this possible precipitation effect, we did not take into consideration the estimated values that coincides with the low-concentration zones (black triangles in Figure 16). Consequently, we based our interpretation on the estimated values that are not located at the low-concentration zones.

The second interesting characteristic of the estimated magnetization distribution along the synthetic sample is about the estimated inclination/declination (Figures 16b and c). Note that the estimated inclinations (blue dots in Figure 16b) within the four prisms forming the sample are close to the approximated values shown in Table 3. On the other hand, the estimated declinations (blue dots in Figure 16c) are close to the values shown in Table 3 at the prisms 0, 1 and 2, but are very different at the prism 3. This discrepancy nonetheless is not a problem because, at prism 3, the estimated inclination is close to $90°$ (Figure 16b) and, in this case, the estimated declinations are not important.

These results show that, even inverting a magnetic data set that were measured by a prototype magnetometer and were, at least apparently, highly contaminated with position noise, our method estimated a magnetization distribution that is consistent with the ARM orientation within our manufactured sample.

5. Conclusion

We have presented a new method for inverting scanning magnetic microscopy data with the purpose of estimating the internal magnetization distribution of a rectangular rock sample whose internal magnetization distribution varies along one of its axes. Our method takes advantage of the geometry of a rectangular sample to propose a new scanning design aiming at providing the magnetic data not only on a single plane over the sample, but on four mutually orthogonal planes located around the sample. The use of magnetic data located on the four planes instead of a single one introduces independent information into the linear system to be solved and consequently leads to a a better conditioned inverse problem.

Results with synthetic data produced by a simulated highly-magnetized sample show not only the good performance of our method in retrieving the magnetization distribution within a rock sample in an ideal case, but also how the results obtained by our method are negatively impacted by imprecisions in the sensor positioning (or position noise). Results with synthetic data produced by a simulated sample that resembles a marine ferro-manganese crust having a complex and heterogeneous internal magnetization distribution suggest that our method could be applied to invert magnetic data produced by real geological samples. We have also applied our method to invert experimental magnetic data for estimating the internal magnetization distribution of a synthetic sample that was manufactured in laboratory. Despite the misalignment problems occurred during the scanning stage and also the apparent high position noise in the experimental magnetic data, our method estimated a meaningful magnetization distribution that is consistent with that one in the manufactured sample.

These results show that our method could be an in-

teresting complement of traditional paleomagnetic techniques aiming at providing a non-destructive diagnostic of geological samples. Nevertheles, further tests using either manufactured and geological samples need to be carried out with the purpose of validating our approach, better evaluating the effects of position noise and misalignment problems during the scanning stage and developing automatic pre-processing techniques. By presuming that the internal magnetization of the rectangular sample varies along one of its axis we implicitly restrict the application of our method to samples that are perpendicular to the growth lamination within rocks. It would be interesting to generalize our method in order to remove this restriction and allow its application to estimate complex magnetization distributions within rock samples.

References

Aster, R. C., B. Borchers, and C. H. Thurber (2005), *Parameter Estimation and Inverse Problems, Volume 90 (International Geophysics)*, Academic Press.

Baratchart, L., D. P. Hardin, E. A. Lima, E. B. Saff, and B. P. Weiss (2013), Characterizing kernels of operators related to thin-plate magnetizations via generalizations of hodge decompositions, *Inverse Problems*, *29*(1), 015,004, doi:10.1088/0266-5611/29/1/015004.

Barnes, G. (2014), Reconstructing the gravity gradient anomaly field from surveys with wide line spacing using equivalent source processing: an error analysis, *Geophysical Prospecting*, *62*(3), 646–657, doi:10.1111/1365-2478.12098.

Barnes, G., and J. Lumley (2011), Processing gravity gradient data, *GEOPHYSICS*, *76*(2), I33–I47, doi:10.1190/1.3548548.

Baudenbacher, F., L. E. Fong, J. R. Holzer, and M. Radparvar (2003), Monolithic low-transition-temperature superconducting magnetometers for high resolution imaging magnetic fields of room temperature samples, *Appl. Phys. Lett.*, *82*(20), 3487–3489, doi:http://dx.doi.org/10.1063/1.1572968.

Cordell, L. (1992), A scattered equivalent-source method for interpolation and gridding of potentialfield data in three dimensions, *GEOPHYSICS*, *57*(4), 629–636, doi:10.1190/1.1443275.

Dampney, C. N. G. (1969), The equivalent source technique, *GEOPHYSICS*, *34*(1), 39–53, doi:10.1190/1.1439996.

Egli, R., and F. Heller (2000), High-resolution imaging using a high-tc superconducting quantum interference device (squid) magnetometer, *J. Geophys. Res.: Solid Earth*, *105*(B11), 25,709–25,727, doi:10.1029/2000JB900192.

Emilia, D. A. (1973), Equivalent sources used as an analytic base for processing total magnetic field profiles, *GEOPHYSICS*, *38*(2), 339–348, doi:10.1190/1.1440344.

Engl, H. W., M. Hanke, and A. Neubauer (1996), *Regularization of Inverse Problems (Mathematics and Its Applications)*, Springer.

Fong, L. E., J. R. Holzer, K. K. McBride, E. A. Lima, F. Baudenbacher, and M. Radparvar (2005), High-resolution room-temperature sample scanning superconducting quantum interference device microscope configurable for geo-

logical and biomagnetic applications, *Rev. Sci. Instrum.*, *76*(5), doi:10.1063/1.1884025.

Fu, R., E. Lima, and B. Weiss (2014), No nebular magnetization in the allende {CV} carbonaceous chondrite, *Earth Planet. Sci. Lett.*, *404*, 54–66, doi: 10.1016/j.epsl.2014.07.014.

Gattacceca, J., M. Boustie, B. P. Weiss, P. Rochette, E. A. Lima, L. E. Fong, and F. J. Baudenbacher (2006), Investigating impact demagnetization through laser impacts and squid microscopy, *Geology*, *34*(5), 333–336, doi: 10.1130/G21898.1.

Guspí, F., and I. Novara (2009), Reduction to the pole and transformations of scattered magnetic data using newtonian equivalent sources, *GEOPHYSICS*, *74*(5), L67–L73, doi:10.1190/1.3170690.

Hankard, F., J. Gattacceca, C. Fermon, M. Pannetier-Lecoeur, B. Langlais, Y. Quesnel, P. Rochette, and S. A. McEnroe (2009), Magnetic field microscopy of rock samples using a giant magnetoresistancebased scanning magnetometer, *Geochem., Geophys., Geosyst.*, *10*(10), doi: 10.1029/2009GC002750.

Hansen, R. O., and Y. Miyazaki (1984), Continuation of potential fields between arbitrary surfaces, *GEOPHYSICS*, *49*(6), 787–795, doi:10.1190/1.1441707.

Kara, I., O. T. Bal, H. Tur, and A. Ates (2014), A new efficient method for topographic distortion correction, analytical continuation, vertical derivatives and using equivalent source technique: Application to field data, *Journal of Applied Geophysics*, *106*, 67–76, doi: 10.1016/j.jappgeo.2014.04.011.

Leão, J. W. D., and J. B. C. Silva (1989), Discrete linear transformations of potential field data, *GEOPHYSICS*, *54*(4), 497–507, doi:10.1190/1.1442676.

Lee, S.-Y., J. Matthews, and F. C. Wellstood (2004), Position noise in scanning superconducting quantum interference device microscopy, *Appl. Phys. Lett.*, *84*(24), 5001–5003, doi: 10.1063/1.1763215.

Li, Y., and D. W. Oldenburg (2010), Rapid construction of equivalent sources using wavelets, *GEOPHYSICS*, *75*(3), L51–L59, doi:10.1190/1.3378764.

Li, Y., M. Nabighian, and D. W. Oldenburg (2014), Using an equivalent source with positivity for low-latitude reduction to the pole without striation, *GEOPHYSICS*, *79*(6), J81–J90, doi:10.1190/geo2014-0134.1.

Lima, E. A., B. P. Weiss, L. Baratchart, D. P. Hardin, and E. B. Saff (2013), Fast inversion of magnetic field maps of unidirectional planar geological magnetization, *J. Geophys. Res.: Solid Earth*, *118*(6), 2723–2752, doi: 10.1002/jgrb.50229.

Lima, E. A., A. C. Bruno, H. R. Carvalho, and B. P. Weiss (2014), Scanning magnetic tunnel junction microscope for high-resolution imaging of remanent magnetization fields, *Measurement Science and Technology*, *25*(10), 105,401, doi:10.1088/0957-0233/25/10/105401.

Mareschal, J. C. (1985), Inversion of potential field data in fourier transform domain, *Geophysics*, *50*(4), 685–691, doi: 10.1190/1.1441943.

Mendonça, C. A. (1992), Interpolação de dados de campo potencial através da camada equivalente, Ph.D. thesis, Universidade Federal do Pará, Belém do Pará, Brazil.

Mendonça, C. A., and J. B. C. Silva (1994), The equivalent data concept applied to the interpolation of potential field data, *GEOPHYSICS*, *59*(5), 722–732, doi: 10.1190/1.1443630.

Mendonça, C. A., and J. B. C. Silva (1995), Interpolation of potentialfield data by equivalent layer and minimum curvature: A comparative analysis, *GEOPHYSICS*, *60*(2), 399–407, doi:10.1190/1.1443776.

Nagy, D., G. Papp, and J. Benedek (2000), The gravitational potential and its derivatives for the prism, *Journal of Geodesy*, *74*(7-8), 311–326, doi:10.1007/s001900000116.

Oda, H., A. Usui, I. Miyagi, M. Joshima, B. P. Weiss, C. Shantz, L. E. Fong, K. K. McBride, R. Harder, and F. J. Baudenbacher (2011), Ultrafine-scale magnetostratigraphy of marine ferromanganese crust, *Geology*, *39*(3), 227–230, doi:10.1130/G31610.1.

Oliveira Jr., V. C., V. C. F. Barbosa, and L. Uieda (2013), Polynomial equivalent layer, *GEOPHYSICS*, *78*(1), G1–G13, doi:10.1190/geo2012-0196.1.

Roth, B. J., N. G. Sepulveda, and J. P. Wikswo (1989), Using a magnetometer to image a two-dimensional current distribution, *J. Appl. Phys. (Melville, NY, U. S.)*, *65*(1), 361–372, doi:10.1063/1.342549.

Silva, J. B. C. (1986), Reduction to the pole as an inverse problem and its application to low-latitude anomalies, *GEOPHYSICS*, *51*(2), 369–382, doi:10.1190/1.1442096.

Tikhonov, A. N., and V. Y. Arsenin (1977), *Solutions of Ill-Posed Problems (Scripta series in mathematics)*, V. H. Winston & Sons.

Uehara, M., and N. Nakamura (2007), Scanning magnetic microscope system utilizing a magneto-impedance sensor for a nondestructive diagnostic tool of geological samples, *Rev. Sci. Instrum.*, *78*(4), doi:10.1063/1.2722402.

Uehara, M., and N. Nakamura (2008), Identification of stable remanence carriers through a magneto-impedance scanning magnetic microscope, *Stud. Geophys. Geod.*, *52*(2), 211–223, doi:10.1007/s11200-008-0014-2.

Usui, Y., M. Uehara, and K. Okuno (2012), A rapid inversion and resolution analysis of magnetic microscope data by the subtractive optimally localized averages method, *Comput. Geosci.*, *38*(1), 145–155, doi:10.1016/j.cageo.2011.05.001.

Van Der Voo, R. (1993), *Paleomagnetism of the Atlantic, Tethys and Iapetus oceans.*

Von Frese, R. R. B., W. J. Hinze, and L. W. Braile (1981), Spherical earth gravity and magnetic anomaly analysis by equivalent point source inversion, *Earth and Planetary Science Letters*, *53*(1), 69 – 83, doi:10.1016/0012-821X(81)90027-3.

Weiss, B. P., E. A. Lima, L. E. Fong, and F. J. Baudenbacher (2007a), Paleointensity of the earth's magnetic field using {SQUID} microscopy, *Earth Planet. Sci. Lett.*, *264*(12), 61–71, doi:10.1016/j.epsl.2007.08.038.

Weiss, B. P., E. A. Lima, L. E. Fong, and F. J. Baudenbacher (2007b), Paleomagnetic analysis using squid microscopy, *J. Geophys. Res.: Solid Earth*, *112*(B9), doi:10.1029/2007JB004940.
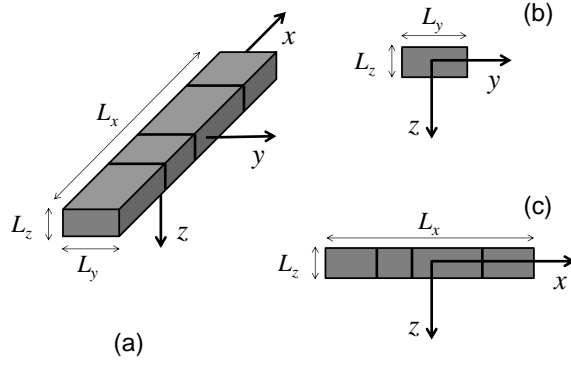
Figure 1. Main coordinate system (MCS). The origin of this coordinate system coincides with the center of the sample (gray prisms and rectangles). The gray juxtaposed prisms represent regions with constant and uniform magnetization. The sample is shown from (*a*) a superior perspective view and also from two side views represented in (*b*) and (*c*).
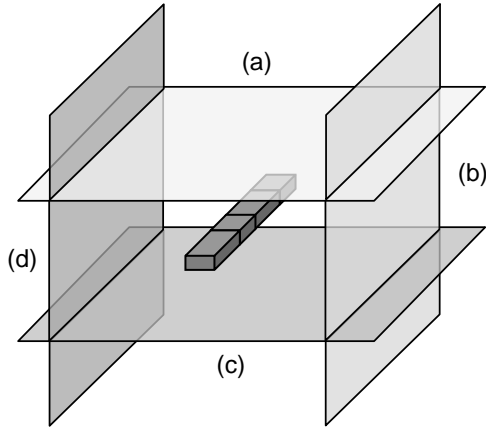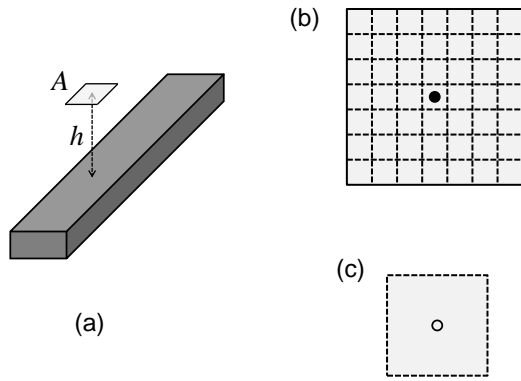

Figure 2. Schematic representation of the rectangular rock sample shown in Figure 1. The gray juxtaposed prisms represent regions with constant and uniform magnetization. The magnetic induction produced by the rock sample is measured on the planes located (*a*) above, (*b*) on the right side, (*c*) below and (*d*) on the left side of the sample. These observation planes are identified, respectively, by the index $\alpha = 0, 1, 2, 3$.
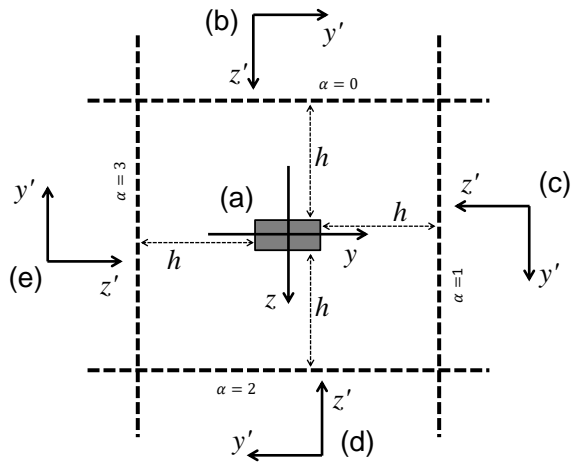
Figure 3. 2D sketch of the coordinate systems. (a) MCS (Figure 1). (b), (c), (d) and (e) Local coordinate systems (LCS's) of the measured magnetic induction on the four observation planes, $\alpha = 0, 1, 2, 3$ (dashed lines), which are located at the same distance h from the surface of the sample. Note that there is a different LCS for the measured magnetic induction on each observation plane (dashed lines). The quantities referred to the LCS's are marked with a prime ($'$). The x-axis of the MCS (Figure 1) coincides with the x'-axes of all LCS's. The x- and x'-axes point into the plane of paper.
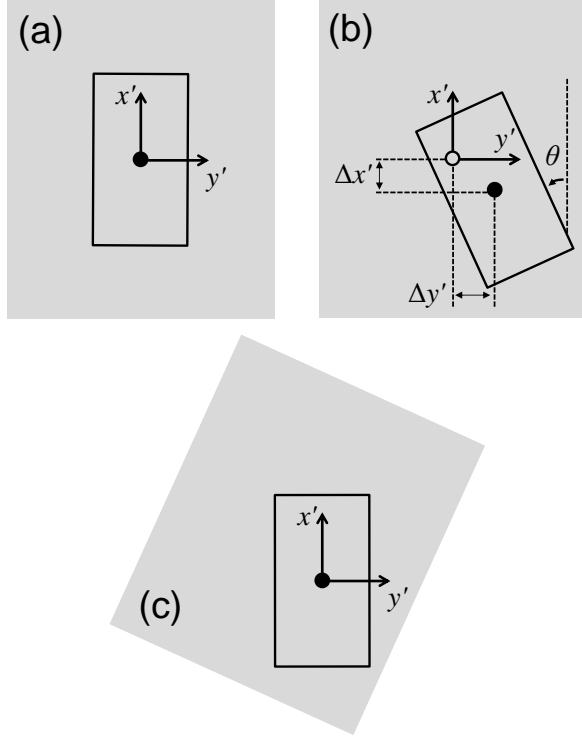
Figure 4. Schematic representation of misalignments during the acquisition of magnetic data. The projections of the edges and the center of the sample onto the observation plane are represented, respectively, by the open rectangles and black dots. The grey rectangles represent the area containing the magnetic data on the observation plane. x' and y' represent the axes and the open dot shown in (b) represents the origin of the LCS (Figure 3). (a) Example of acquisition without misalignment. In this case, the center of the sample coincides with the origin of the LCS and the edges of the sample are aligned with the axes of the LCS. (b) Example of acquisition presenting misalignments. In this case, the relative position of the center of the sample with respect to the origin of the LCS is displaced by $\Delta x'$ and $\Delta y'$ along, respectively, the x' and y' axes. Besides, the edges of the sample are rotated anticlockwise with respect to the axes of the LCS. (c) Corrected position of the sample with respect to the magnetic data obtained on the observation plane.

Figure 5. Schematic representation of the integral **??**.
(a) Magnetic sensor with active area A (light grey square)
located at a distance h of the sample (grey prism). (b)
Detailed representation of the sensor active area, which
is centered at the observation point (x_i, y_i) (black circle).
The square active area is discretized into a regular grid
of Q square cells (limited by the dashed lines). (c) jth
cell with area ΔA and center at the point (x_j, y_j) (open
circle), $j = 1, ..., Q$.
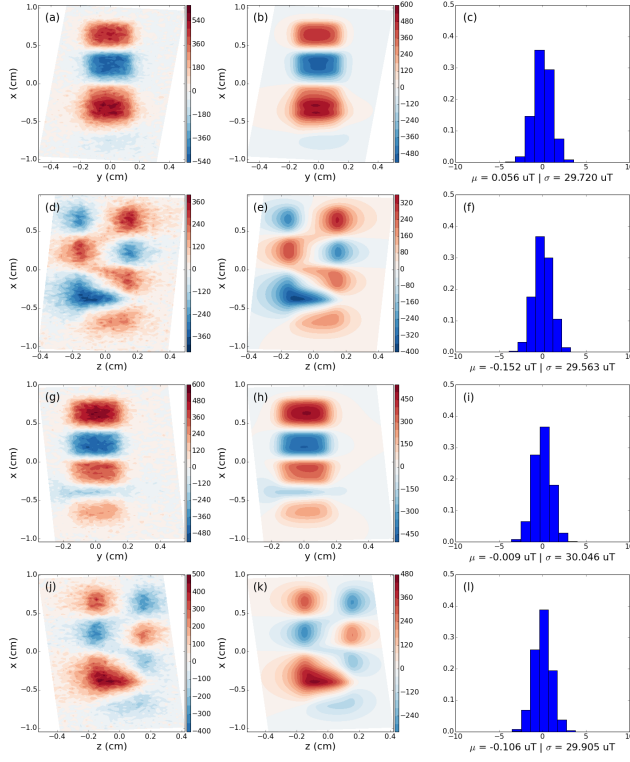
Figure 6. Validation test. (a), (d), (g) and (j) Noise-corrupted magnetic data produced by the synthetic sample (not shown) on the observation planes $\alpha = 0, 1, 2$ and 3, respectively. (b), (e), (h), (k) Predicted data produced by the estimated magnetization distribution obtained by inversion on the observation planes $\alpha = 0, 1, 2$ and 3, respectively. (c), (f), (i) and (l) Normalized histograms of the residuals between the predicted data shown in (b), (e), (h), (k) and the noise-corrupted magnetic data shown in (a), (d), (g), (j). The normalization consists in subtracting from the residuals its sample mean μ and dividing the result by its sample standard deviation σ. The values are in μT.

Figure 7. Validation test. Comparison between the true (red dots) and estimated (blue dots) magnetization (a) intensity, (b) inclination and (c) declination. The values are plotted along the x-axis, at the center of each prism forming the interpretation model. The black dashed lines in (b) and (c) indicate the $0°$ value.
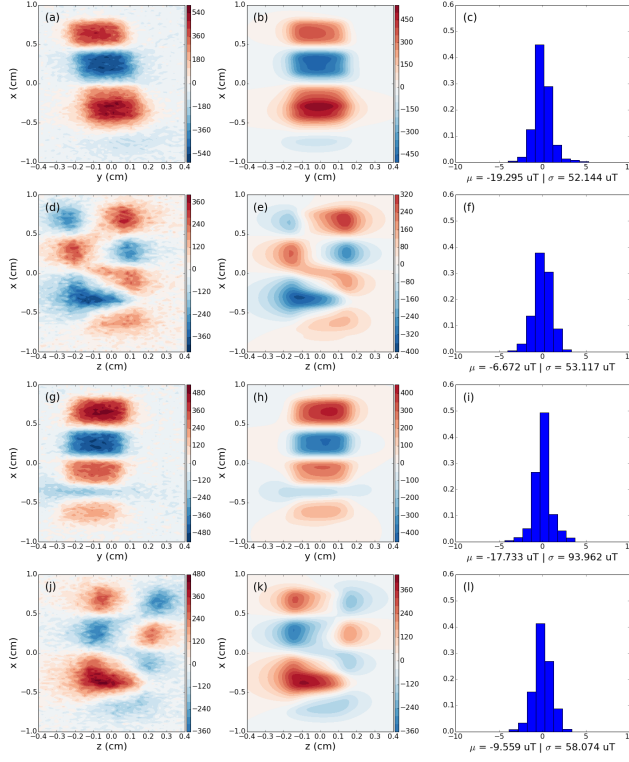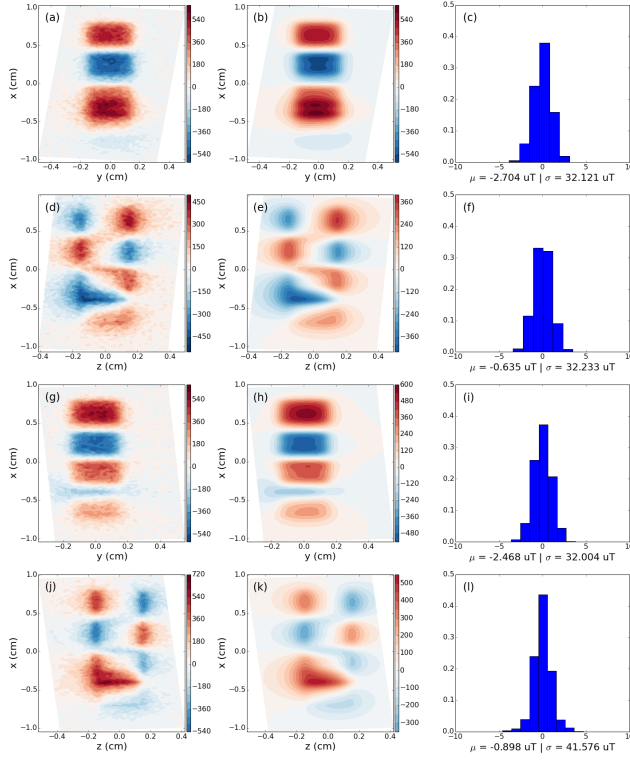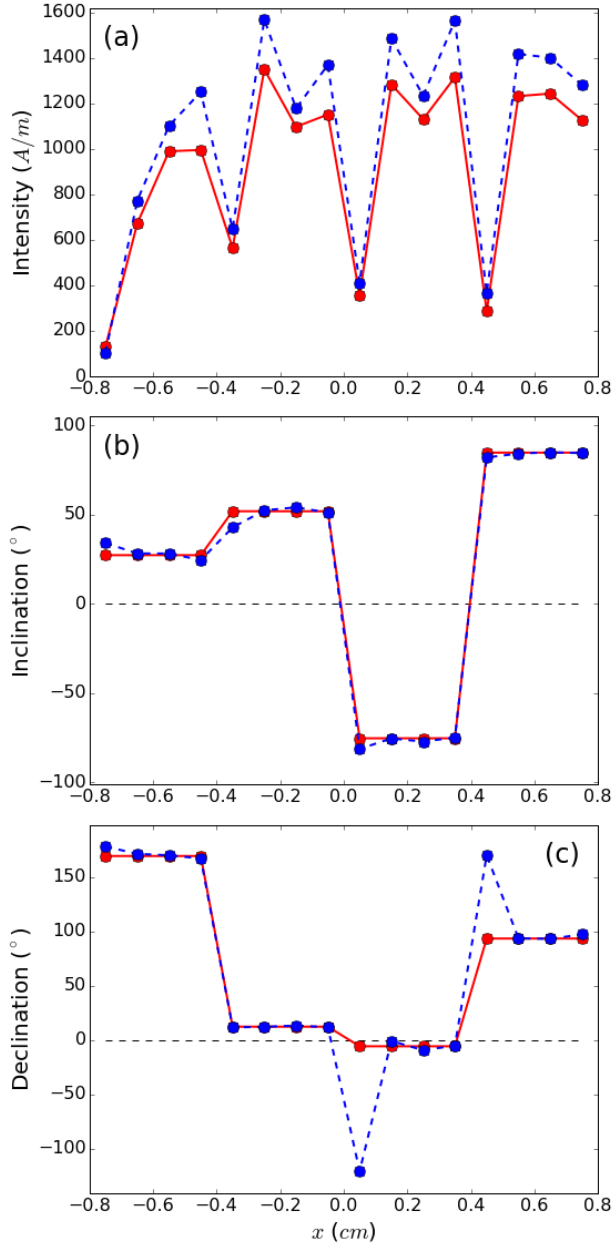
Figure 8. Pre-processing errors test. (a), (d), (g) and (j) Noise-corrupted magnetic data produced by the synthetic sample (not shown) on the observation planes $\alpha = 0, 1, 2$ and 3, respectively. (b), (e), (h), (k) Predicted data produced by the estimated magnetization distribution obtained by inversion on the observation planes $\alpha = 0, 1, 2$ and 3, respectively. (c), (f), (i) and (l) Normalized histograms of the residuals between the predicted data shown in (b), (e), (h), (k) and the noise-corrupted magnetic data shown in (a), (d), (g), (j). The normalization consists in subtracting from the residuals its sample mean μ and dividing the result by its sample standard deviation σ. The values are in μT.

Figure 9. Pre-processing errors test. Comparison between the true (red dots) and estimated (blue dots) magnetization (a) intensity, (b) inclination and (c) declination. The values are plotted along the x-axis, at the center of each prism forming the interpretation model. The black dashed lines in (b) and (c) indicate the $0°$ value.

Figure 10. Sensor-to-sample distance test. (a), (d), (g) and (j) Noise-corrupted magnetic data produced by the synthetic sample (not shown) on the observation planes $\alpha = 0, 1, 2$ and 3, respectively. (b), (e), (h), (k) Predicted data produced by the estimated magnetization distribution obtained by inversion on the observation planes $\alpha = 0, 1, 2$ and 3, respectively. (c), (f), (i) and (l) Normalized histograms of the residuals between the predicted data shown in (b), (e), (h), (k) and the noise-corrupted magnetic data shown in (a), (d), (g), (j). The normalization consists in subtracting from the residuals its sample mean μ and dividing the result by its sample standard deviation σ. The values are in μT.

Figure 11. Sensor-to-sample distance test. Comparison between the true (red dots) and estimated (blue dots) magnetization (a) intensity, (b) inclination and (c) declination. The values are plotted along the x-axis, at the center of each prism forming the interpretation model. The black dashed lines in (b) and (c) indicate the 0° value.
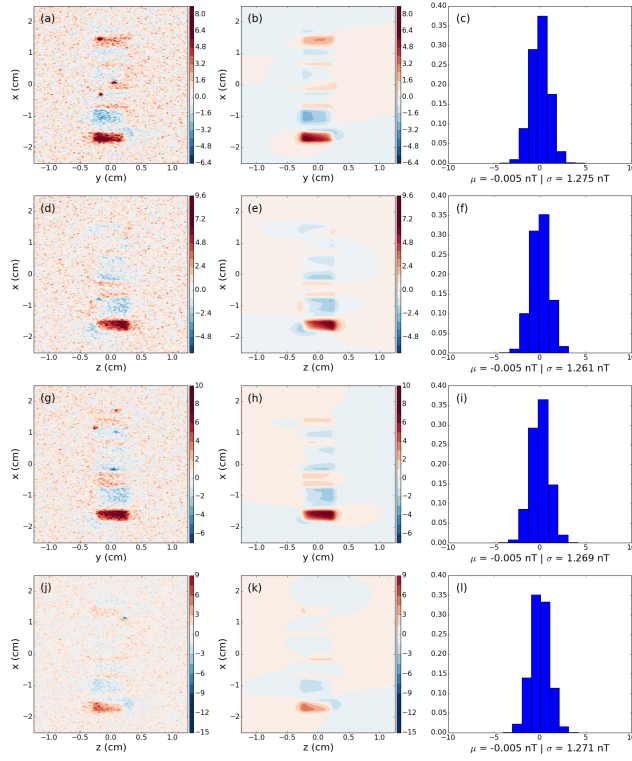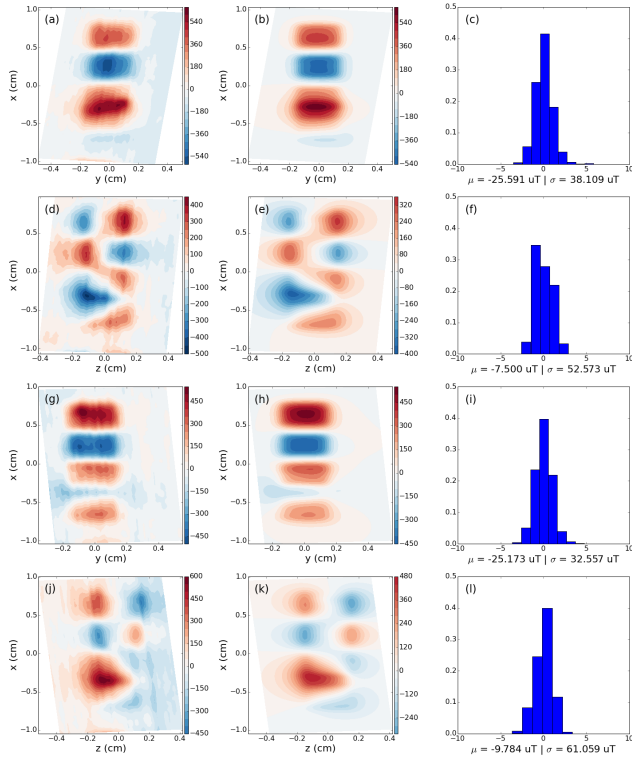
Figure 12. Marine ferro-manganese crust sample. (a), (d), (g) and (j) Noise-corrupted magnetic data produced by the synthetic sample (not shown) on the observation planes $\alpha = 0, 1, 2$ and 3, respectively. (b), (e), (h), (k) Predicted data produced by the estimated magnetization distribution obtained by inversion on the observation planes $\alpha = 0, 1, 2$ and 3, respectively. The color scales are slightly saturated for improving the visualization. (c), (f), (i) and (l) Normalized histograms of the residuals between the predicted data shown in (b), (e), (h), (k) and the noise-corrupted magnetic data shown in (a), (d), (g), (j). The normalization consists in subtracting from the residuals its sample mean μ and dividing the result by its sample standard deviation σ. The values are in nT.
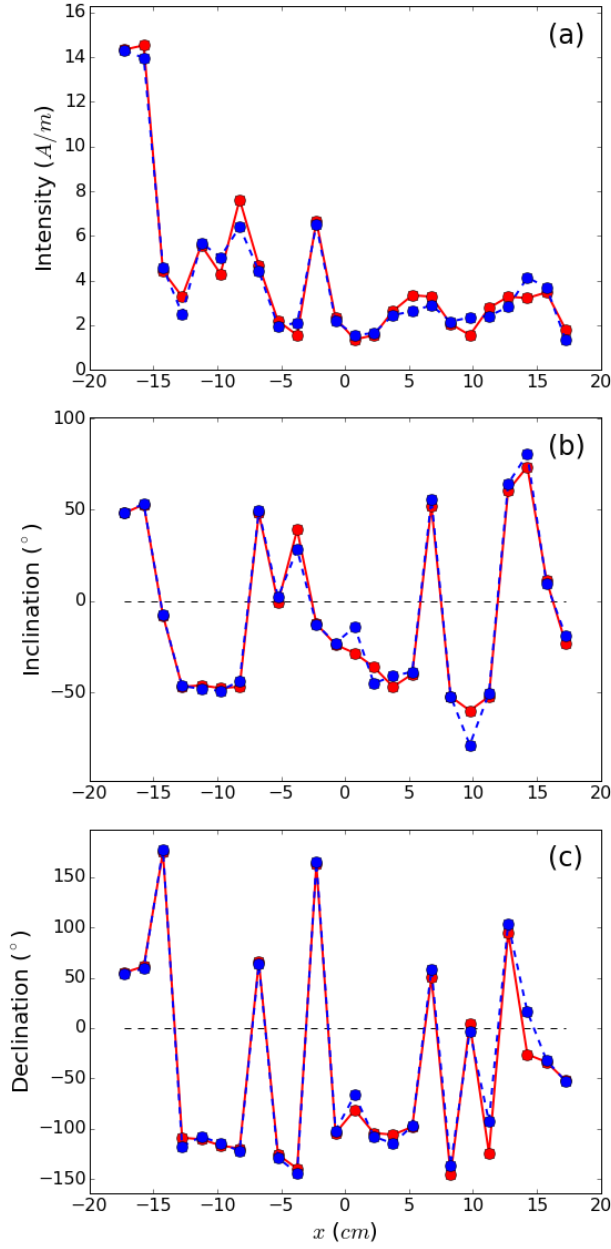
Figure 13. Marine ferro-manganese crust sample. Comparison between the true (red dots) and estimated (blue dots) magnetization (a) intensity, (b) inclination and (c) declination. The values are plotted along the x-axis, at the center of each prism forming the interpretation model. The black dashed lines in (b) and (c) indicate the $0°$ value.
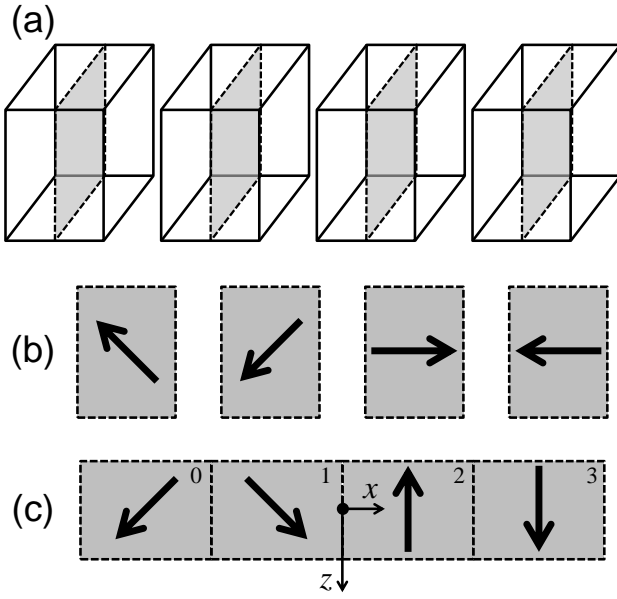
Figure 14. Manufactured sample. (a) Four prisms forming the sample. The ARM magnetization of these prisms are approximately parallel to the vertical planes represented in grey. (b) Magnetization (thick arrows) of the prisms on the vertical planes shown in (a). (c) Resultant sample obtained by juxtaposing the magnetized prisms. The numbers indicate the index of each prism, whose magnetization is represented by the thick arrows. The inclination and declination values of the ARM within each prism is shown in Table 3. The resulting sample is referred to a MCS (Figure 1) with origin represented by the black dot and axes x and z represented by the thin arrows.

Figure 15. Application to real data. (a), (d), (g) and (j) Observed magnetic data produced by the synthetic sample (not shown) on the observation planes $\alpha = 0, 1, 2$ and 3, respectively. (b), (e), (h), (k) Predicted data produced by the estimated magnetization distribution obtained by inversion on the observation planes $\alpha = 0, 1, 2$ and 3, respectively. (c), (f), (i) and (l) Normalized histograms of the residuals between the predicted data shown in (b), (e), (h), (k) and the observed magnetic data shown in (a), (d), (g), (j). The normalization consists in subtracting from the residuals its sample mean μ and dividing the result by its sample standard deviation σ. The values are in μT.
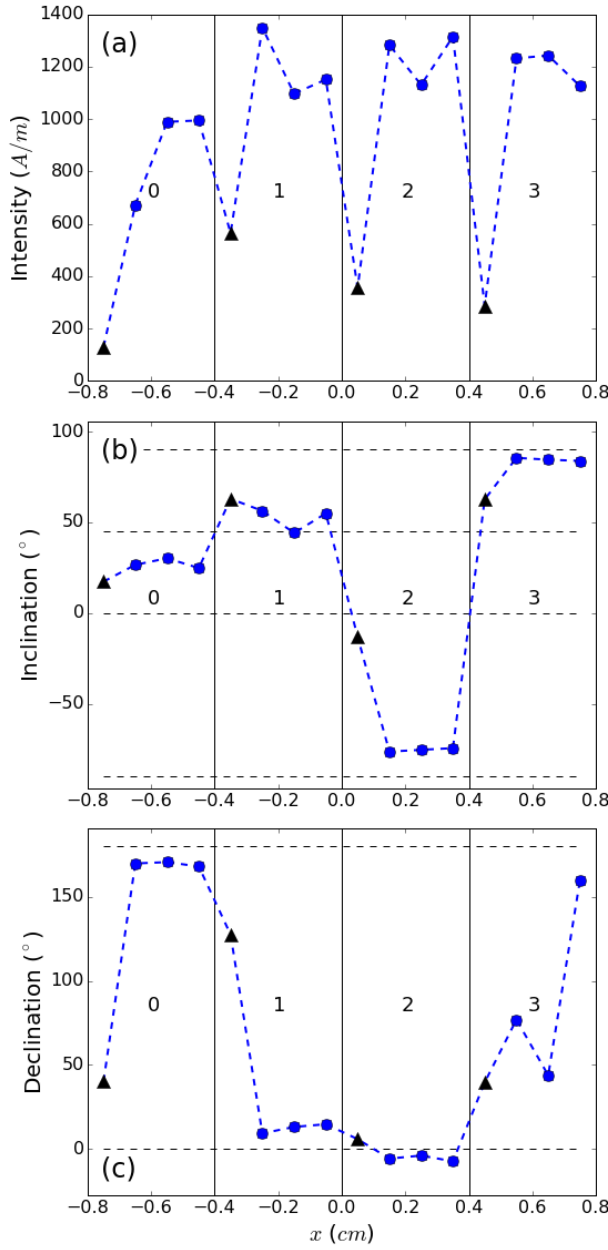
Figure 16. Application to real data. Estimated magnetization (a) intensity, (b) inclination and (c) declination. The values are plotted along the x-axis, at the center of each prism forming the interpretation model. The continuous (vertical) black lines divide the estimated values representing each prism forming the sample. The numbers indicate the index of each prism (Figure 14c and Table 3. The black dashed (horizontal) lines in (b) indicate the values $-90°$, $0°$, $45°$ and $90°$. The black dashed (horizontal) lines in (c) indicate the values $0°$ and $180°$. The estimated values that are represented by black triangles are considered spurious due to the magnetite precipitation.

Table 1. Transformations between the LCS's and the MCS[a]

	Cartesian coordinate		Field component	
α	y	z	y	z
0	y'	z'	$-$	z'
1	$-z'$	y'	$-z'$	$-$
2	$-y'$	$-z'$	$-$	$-z'$
3	z'	$-y'$	z'	$-$

[a] Correspondence between the Cartesian coordinates y' and z' and the Cartesian coordinates y and z as well as between the z'-component and the y- or z-component of the magnetic induction. The quantities marked with prime ($'$) are referred to the LCS's (Fig. 3b-e) while the quantities without prime ($'$) are referred to the MCS (Fig. 3a).

Table 2. Misalignment parameters[a]

α	θ (°)	$\Delta x'$ (μm)	$\Delta y'$ (μm)
0	5.5	0	-100
1	3.0	500	-400
2	3.0	200	1000
3	4.0	200	500

[a] Parameters θ, $\Delta x'$ and $\Delta y'$ (Figure 4b) defining the misalignments in the magnetic data produced by the synthetic sample described in section 3.

Table 3. Approximated ARM orientation within the prisms forming synthetic sample[a]

index	I (°)	D (°)
0	45	180
1	45	0
2	-90	$-$
3	90	$-$

[a] ARM inclination (I) and declination (D) of the prisms forming the synthetic sample that was manufactured in laboratory. Each prism is indicated by an index, according to the Figure 14c.